Journal of Alloys and Compounds 489 (2010) 64–71

Contents lists available at ScienceDirect

Journal of Alloys and Compounds

journal homepage: www.elsevier.com/locate/jallcom

Synthesis, characterization, and property studies of (La, Ag) FeO_3 ($0.0 \leq x \leq 0.3$) perovskites

Manjunath B. Bellakki, Brandon J. Kelly, V. Manivannan*

Department of Mechanical Engineering, Colorado State University, Fort Collins, Colorado 80523, USA

ARTICLE INFO

Article history:
Received 31 January 2009
Received in revised form 8 August 2009
Accepted 14 August 2009
Available online 22 August 2009

Keywords:
Oxide materials
Chemical synthesis
Crystal structure
Magnetic measurements
X-ray diffraction

ABSTRACT

Applying a solution – based combustion process, Ag-doped $LaFeO_3$ orthoferrites were synthesized. The samples were characterized by multiple techniques to establish structure – property relationships. Specifically, for structural characterization, powder X-ray diffraction (XRD), scanning electron microscopy (SEM), energy dispersive X-ray analysis (EDX), Fourier transmission infrared spectroscopy (FTIR), Thermo-gravimetric analysis (TGA), and X-ray photoelectron microscopy (XPS) were carried out. For properties, squid magnetometer measurements (for magnetic properties), titrations (for chemical analysis), and diffuse reflectance (for optical band gap properties) measurements were carried out to elucidate structure–property relationship.

1. Introduction

Perovskite-oxides such as $LaFeO_3$ have found applications in several technologies mainly due to their unique structural features [1–7]. The properties of such materials are influenced by the type and amount of doping, as well as the synthesis procedure employed to process these materials. Accordingly, the literature describes several known procedures to make the perovskite material in general, such as solid-state reaction [8], co-precipitation [9], combustion [10], polyaol [11], citrate–gel [12], hydrothermal [13], sol–gel [14], and microemulsion [15] methods.

The key for $LaFeO_3$ to be a potential material for several applications, such as in solid oxide fuel cells (SOFCs), is the mixed conductivity (electronic + ionic) property, due to the presence of mixed valences of Fe^{3+}/Fe^{4+}, accompanied by oxygen non-stoichiometry of the materials. Creation of mixed valency is facilitated by appropriate chemical doping into the $LaFeO_3$ system. Accordingly, Huang et al. found that bivalent Sr^{2+} substitution into $LaFeO_3$ materials makes them a candidate cathode material in SOFC [16]. We have been motivated to study the effect of monovalent Ag^+ doping into a $LaFeO_3$ system, study the changes in properties, and correlate those property changes to the structural changes. In addition to synthesize such (La, Ag)FeO_3 compounds we have applied a combustion method of synthesis using glycine as a fuel, which has distinct advantages such as having a low temperature process, shorter reaction time, high quality single phase material output, etc., [17,18]. Such an investigation, i.e., examination of the properties of $LaFeO_3$-doped with Ag^+ and synthesized by solution–combustion method using glycine as fuel, has not been reported so far.

2. Experimental

$La_{1-x}Ag_xFeO_3$ ($0 \leq x \leq 0.3$) solid solutions were prepared by dissolving stoichiometric amounts of metal nitrates in a minimum amount of water in a Pyrex dish. A calculated amount of glycine fuel was added. The resulting aqueous solution was introduced into a muffle furnace maintained at 400 °C. The mixture boiled, followed by frothing, and ignited with evolution of a large amount of gases. The mixture ignited and caught fire to give a voluminous combustion product. Assuming complete combustion, the general equation for the formation of samples can be proposed as follows:

$$(_{1-x})La(NO_3)_3 + xAg(NO_3)_2 + Fe(NO_3)_3 + C_2H_5NO_2 \rightarrow La_{1-x}Ag_xFeO_3 + CO_2 + H_2O(g) + N_2(g) \quad (1)$$

The phase purity and crystal structure were examined by a Bruker X-ray diffractometer using Cu Kα radiation with a nickel filter. For Rietveld refinement, data was collected at a scan rate of 0.5°/min with a 0.02° step size for 2θ from 10° to 100°. The morphology of the powder was examined using a JEOL JSM-840A scanning electron microscope fitted with an energy dispersive X-ray analyzer (EDX). Infrared spectra of samples were recorded on a Thermo Nicolet FT-IR Spectrometer for a spectrum from 400 cm^{-1} to 4000 cm^{-1}. The magnetization measurements were performed using a SQUID magnetometer in the temperature range 2.5–300 K with a static applied field of 1000 Oe. Diffuse reflectance spectra were recorded in the wavelength range 250–2500 nm using a Varian Associated Cary 500 double beam spectrophotometer. Compressed polytetrafluoroethylene (PTFE) was used for standard calibration (100%, reflectance). XPS experiments were performed on a Physical Electronics 5800 spectrometer. This system has a monochromatic Al Kα X-ray source (h_α = 1486.6 eV), hemispherical analyzer, and a multichannel detector. A low energy (30 eV) electron

* Corresponding author. Tel.: +1 970 491 2207; fax: +1 970 491 3681.
E-mail address: mani@engr.colosate.edu (V. Manivannan).

0925-8388/$ – see front matter © 2009 Published by Elsevier B.V.
doi:10.1016/j.jallcom.2009.08.059

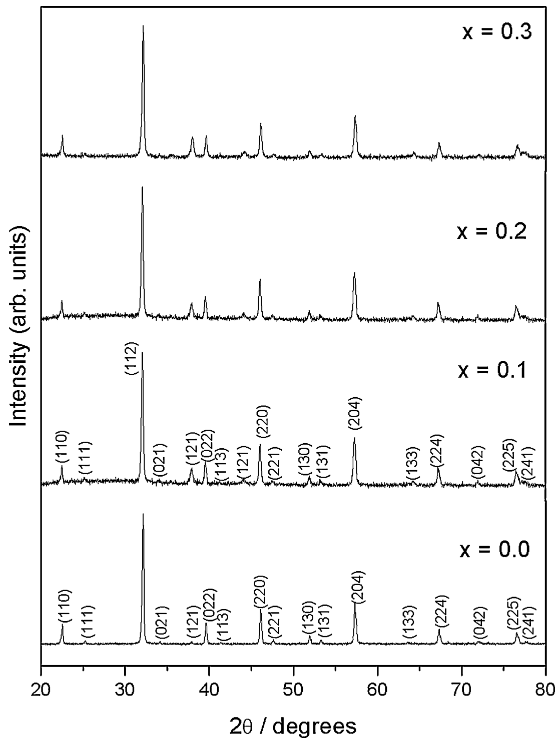

Fig. 1. Powder XRD patterns of $La_{1-x}Ag_xFeO_3$ ($0.0 \leq x \leq 0.3$) phases.

gun was used for charge neutralization on the non-conducting samples. The binding energy (BE) scales for the samples were referenced to the carbon 1 s peak at 284.8 eV. Thermo-gravimetric analysis (TGA) was performed using the weight and temperature calibrated TA instruments 2950. The sample was heated in a platinum pan with a heating rate of 5 °C/min to reach the final temperature.

3. Results and discussion

3.1. Structural characterization

Powder XRD patterns of $La_{1-x}Ag_xFeO_3$ ($0 \leq x \leq 0.3$) solid solutions are shown in Fig. 1. All the samples were single phase in comparison with the reported pattern in the literature (JCPDF No. 01-070-7777), and accordingly were indexed. (La, Ag)FeO_3 crystallizes to an orthorhombic structure with the space group *Pbnm* no.62. The structural details of the system were determined by applying the Rietveld method using the *FullProf* program [19]. In Fig. 2, the observed, calculated, and difference XRD patterns of the typical refined XRD patterns of (a) $LaFeO_3$, and (b) $La_{0.8}Ag_{0.2}FeO_3$ compounds are given. There is a good agreement between observed and calculated patterns. The refined structural parameters, selected bond lengths and bond angles are summarized for all the samples in Table 1. We tried to synthesize the samples with $x > 0.3$, but an impurity, AgO, was observed in these phases. Consequently, we have focused on substitution levels of Cd into $LaFeO_3$ of only up to 30%.

3.2. Microstructure characterization

To gain an understanding of the micro structural features of the synthesized materials, SEM was performed (Fig. 3). SEM showed the microstructure consisting of submicron size particles. The particles of $LaFeO_3$ (Fig. 3a) and $(La_{0.8}Ag_{0.2})FeO_3$ (Fig. 3b) are agglomerated and already connected together to form a porous or open structure. EDX in combination with SEM showed the synthesized ceramics have homogeneous composition (Fig. 4).

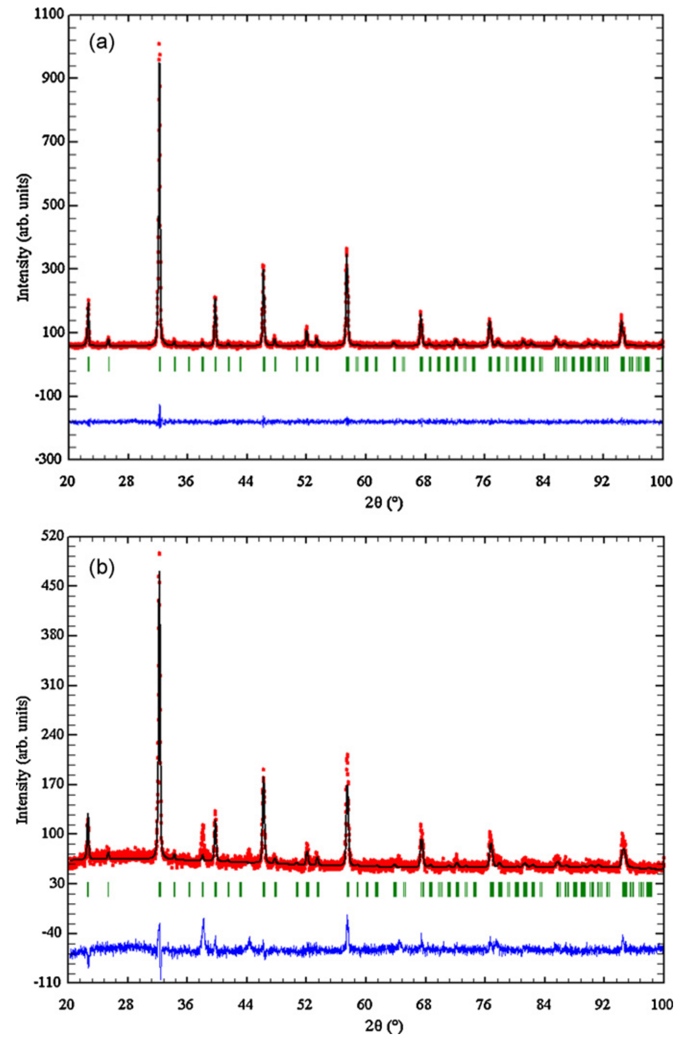

Fig. 2. Typical, observed, calculated, and difference Rietveld – refined XRD. patterns of (a) $LaFeO_3$, and (b) $La_{0.80}Ag_{0.20}FeO_3$.

3.3. Infrared spectroscopy

Fig. 5 shows the FTIR spectra of the parent and Ag-doped samples. The bands in the wave number region 650–500 and 450–400 cm^{-1} arise from the asymmetric stretching vibrations of Fe–O–Fe bonds and deformation of FeO_6 octahedra, respectively [20]. The higher frequency band at 600 cm^{-1} was assigned to the Fe–O stretching vibration mode which involves internal motion of a change in Fe–O bond length, and the lower band around 450 cm^{-1} corresponds to the bending mode, which is sensitive to a change in the Fe–O–Fe bond angle. Increasing the Ag content did not result in significant shift of the IR data.

3.4. X-ray photoelectron spectroscopy

X-ray photoelectron spectroscopy of parent and silver-substituted $LaFeO_3$ has been recorded to determine the electronic structure (Fig. 6). The binding energies for La 3d, Fe 2p, O 1s, and Ag 3d core-levels are summarized for all the samples in Table 2. Fig. 6 (a, b, c, and d) displays the typical X-ray photoelectron core-level spectra La 3d, Fe 2p, O 1s, and Ag 3d orbits for $La_{1-x}Ag_xFeO_3$ ($0 \leq x \leq 0.3$) samples. In Fig. 6(a), for $x = 0$, the main La 3d peaks are observed at binding energies of 834.16 eV and 851.32 eV, which is consistent with the reported values [21,22], and the satellite peaks (*) at higher binding energies are due to the shake-up state of La

Table 1
Rietveld refined structural parameters for $La_{1-x}Ag_xFeO_3$ (0 < *x* < 0.3) phases.

Compounds Crystal system space group	$LaFeO_3$	$La_{0.90}Ag_{0.10}FeO_3$ Orthorhombic *Pbnm* (62)	$La_{0.80}$ $Ag_{0.20}FeO_3$	$La_{0.70}Ag_{0.70}FeO_3$ Orthorhombic *Pbnm* (62)
Lattice parameters				
a (Å)	5.554(2)	5.552(4)	5.547(7)	5.533(3)
b(Å)	5.562(3)	5.557(5)	5.556(1)	5.544(3)
c(Å)	7.852(4)	7.851(3)	7.848(4)	7.844(2)
Cell volume ($Å^3$)	242.562(3)	242.263(4)	241.930(6)	240.614(6)
La/Ag				
x	0.9955(2)	0.995 (2)	0.9953 (3)	0.9927(4)
y	0.0286(4)	0.029(5)	0.0293 (2)	0.0266(6)
z	0.2500	0.2500	0.2500	0.25
Fe				
x	0.0000	0.0000	0.0000	0
y	0.5000	0.5000	0.5000	0.5
z	0.0000	0.0000	0.0000	0
O_1				
x	0.0730(3)	0.0731(9)	0.0734 (3)	0.0709(10)
y	0.4847(4)	0.4850 (4)	0.4849(2)	0.4875(8)
z	0.2500	0.2500	0.2500	0.25
O_2				
x	0.7152(7)	0.7182(5)	0.7191(7)	0.7197(13)
y	0.2866(6)	0.2892 (9)	0.2901(7)	0.2894(8)
z	0.0376(5)	0.0381(7)	0.0389(5)	0.0382(8)
R-factors (%)				
RP	4.49	4.71	6.25	7.99
RWP	5.59	6.00	8.29	11.9
RBragg	2.79	6.41	19.8	15.3
RF	5.22	7.37	18.3	16.2
χ^2	0.21	0.24	0.43	0.97
Bond lengths				
$Fe_1–O_1$	2.0062(3)	2.0060(4)	2.0056(7)	2.0032(7)
$Fe_1–O_2$	1.9995(4)	1.9772(5)	1.9700(4)	1.9674(6)
$Fe_1–O_2'$	2.0141(3)	2.0346(6)	2.0416(6)	2.0489(9)
Bond angles				
$Fe–O_1–Fe$	156.166(2)	156.161(5)	156.074(4)	155.674(6)
$Fe–O_2–Fe$	156.579(4)	156.469(3)	156.206(6)	156.049(8)

3d, resulting from a core hole with an electron transferred from the O 2p valence band to an empty La 4f orbit [23,24]. The Fe 2p peaks appear at binding energies of 710.49 eV and 724.05 eV (Fig. 6(b), *x* = 0), and are attributed to the spin–orbit splitting of the Fe 2p components [25,26]. The O 1s spectra show one large peak with a binding energy of 530.35 eV, which is consistent with the reported value [25]. The Ag 3d peaks appear at 368.13 and 374.13 eV [26] for *x* = 0.3, indicating Ag is in the +1 state. Shifts in the binding energy were observed due to Ag substitution.

3.5. UV–vis diffuse reflectance spectroscopy

In order to determine the band structure details of (La, Ag) FeO_3 ceramics in conjugation with structural features, DR measurements were carried out. Specifically, the optical band gap of $La_{1-x}Ag_xFeO_3$ ($0 \le x \le 0.3$) was determined (Fig. 7). Fig. 7a shows the diffuse reflectance spectra of $La_{1-x}Ag_xFeO_3$ ($0 \le x \le 0.3$) samples in the UV–vis–NIR range. The diffuse reflectance data was used to calculate the absorption coefficient from the Kubelka–Munk (KM) [27,28] function, defined as:

$$F(R_\infty) = \frac{\alpha}{S} = \frac{(1-R_\infty)^2}{2R} \quad (2)$$

where $R_\infty = R_{sample}/R_{PTFE.}$

Here α is the absorption coefficient, *S* is the scattering coefficient, and $F(R_\infty)$ is the KM function. The energy dependence of the material in the UV–vis–NIR was further explored. The energy dependence of semiconductors near the absorption edge is expressed as:

$$\alpha E = K(E - E_g)^\eta \quad (3)$$

Here *E* is the incident photon energy ($h\nu$), E_g the optical absorption edge energy, *K* a constant, and the exponent η is dependent on the type of optical transition as a result of photon absorption [29]. The exponent η is assigned a value of 1/2, 3/2, 2, and 3 for direct allowed, direct forbidden, indirect allowed, and indirect forbidden transition, respectively [30].

For the diffuse reflectance spectra, the KM function can be used instead of α for estimation of the optical absorption edge energy [29]. It was observed that, for a plot of $F(R_\infty)$, *E* vs. *E* was linear near the edge for direct allowed transition ($\eta = 1/2$). The intercept of the line on abscissa ($F(R_\infty)E = 0$) gave the value of the optical absorption edge energy. The values are determined to be 2.4 ± 0.2, 2.1 ± 0.2, 1.8 ± 0.2, and 1.65 ± 0.2 eV for *x* = 0, 0.1, 0.2, and 0.3, respectively. Fig. 7b shows the plot of the same. The low band gap values indicate these materials can have higher photocatalytic activity compared to the TiO_2 standard material, which has poor catalytic efficiency due to its wide band gap (3.2 eV) [31]. The diffuse reflectance spectra for direct band gap orthorhombic (β) [32] prepared by heating Ta metal in air are also recorded for comparison. The value of optical absorption edge energy for the indirect allowed transition for Ta_2O_5 was found to be 4.0 ± 0.2 eV, which is consistent with those seen for the β-Ta_2O_5 reported [33].

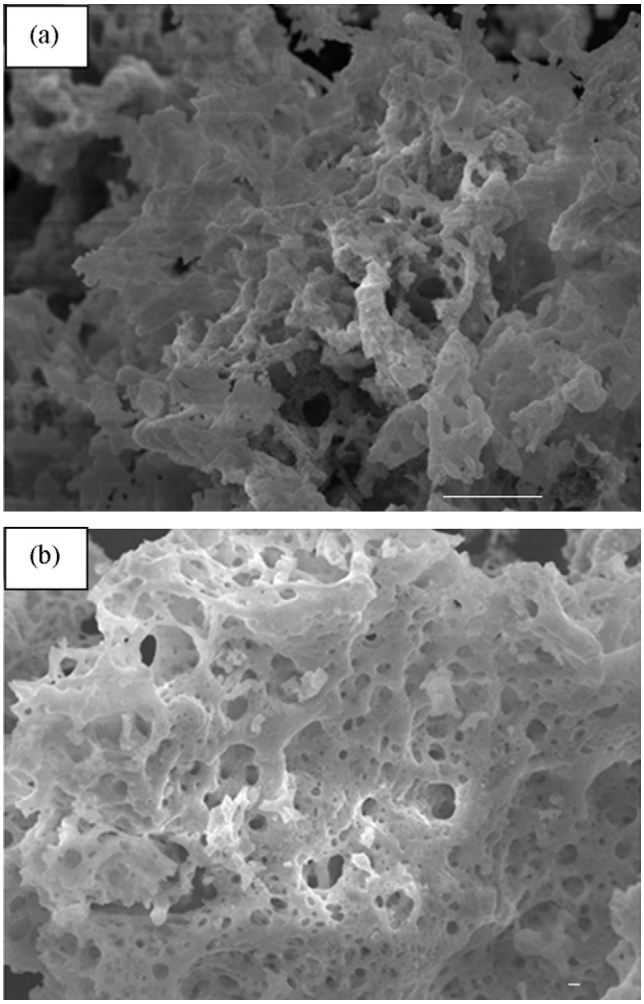

Fig. 3. Scanning electron micrographs of (a) $LaFeO_3$, and (b) $La_{0.80}Ag_{0.20}FeO_3$. The scale bars on the micrographs are 10 μm for (a), and 1 μm for (b), respectively.

3.6. Optical properties

In an analysis of optical band gaps of $LaMO_3$ perovskites (M = Sc, Ti, V, Cr, Mn, Fe, Co Ni, and Cu) [34], reflectivity measurements have shown the optical band gap energy of the materials to be (E_{gap}) ~2 eV. The DR measurements of our compounds determined the band gap to be ~2 eV, which is in agreement with those values. In the same series of compounds, the authors have observed that the nature of the conductivity is of Mott–Hubbard type (for Sc, Ti, V) and the crossover occurs at Cr to that of charge-transfer type. The charge-transfer (CT) energy is strongly dependent on the Fe–O–Fe bond angle, and when it deviates from an ideal Fe–O–Fe bond angle of 180°, the CT energy decreases, resulting in lower E_g values, a situation encountered in (La, Ag) FeO_3 compounds. The electronic transitions are primarily attributed to the conduction band (O 2p to Fe 3d) (Fig. 8). Thus the optical spectroscopy measurements showed that (La, Ag) FeO_3 materials are narrow band gap materials.

Table 2
Binding energies (eV) of core-levels for $La_{1-x}Ag_xFeO_3$ ($0 < x < 0.3$) phases.

Compounds	La $3d_{5/2}$	Fe $2p_{3/2}$	Ag $3d_{5/2}$
$x = 0$	834.16	710.49	–
$x = 0.1$	834.86	711.23	369.31
$x = 0.2$	834.46	711.18	368.72
$x = 0.3$	834.19	710.79	368.13

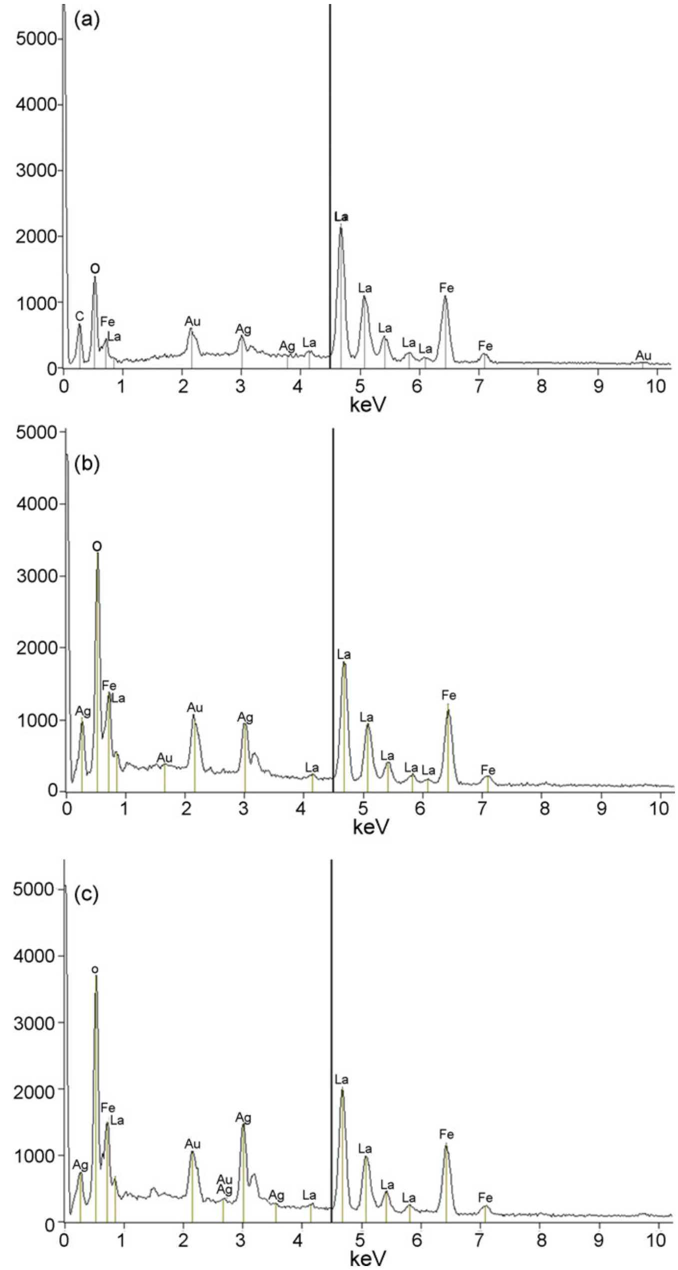

Fig. 4. EDX spectra of Ag-doped $LaFeO_3$ materials: (a) $La_{0.9}Ag_{0.1}FeO_3$, (b)$La_{0.8}Ag_{0.2}FeO_3$, and (c) $La_{0.7}Ag_{0.3}FeO_3$.

3.7. Magnetic property study

Fig. 9 shows the magnetization results for the $La_{1-x}Ag_xFeO_3$ ($0.0 \le x \le 0.3$) samples. Fig. 9(a) shows the temperature dependence of the molar magnetic susceptibility (χ_M) at a magnetic field of 1000 Oe. The χ_M for the parent compound is nearly zero, and at a specific temperature, the susceptibility increases with increasing x. Fig. 9(b) shows the magnetization M as a function of applied field for the $x = 0$ and 0.3 samples at 25 K as indicated. The hysteresis loop for the parent compound originates from the canted anti-parallel Fe^{3+} spins. The loop for the $x = 0.3$ sample shows a nearly similar profile other than an increase in the M values at a field point. The increase in the magnetization with doping is consistent with the data in Fig. 8(a).

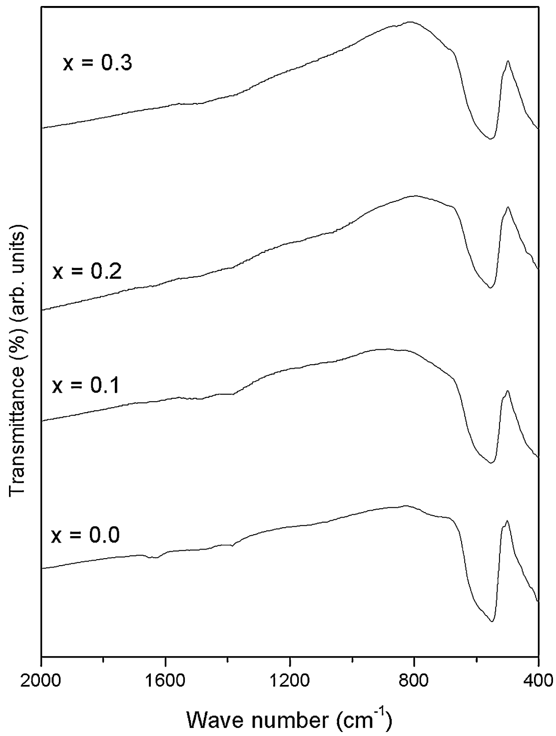

Fig. 5. FTIR spectra of $La_{1-x}Ag_xFeO_3$ ($0.0 \le x \le 0.3$) phases.

Table 3
Values of tolerance factor, magnetic susceptibility and magnetic moment of $La_{1-x}Ag_xFeO_3$ ($0 \le x \le 0.3$) phases.

$La_{1-x}Ag_xFeO_3$	Tolerance factor (t)	χ_M (at 2.5 K)	μ_B (at 2.5 K)$_{BM}$
$x=0$	0.948	0.035	0.031
$x=0.1$	0.943	0.349	0.312
$x=0.2$	0.937	0.452	0.306
$x=0.3$	0.932	0.548	0.491

3.8. Discussion

With Ag doping in $LaFeO_3$ the observed changes in the magnetic and optical properties are correlated to the structural changes in the perovskite system. Magnetic characterization results showed three important features: (a) Magnetic moment of the undoped compound is nearly zero, (b) Magnetization increased with increased Ag doping, and (c) Magnetic moment increased as amount of Ag doping increased.

It is well established in the literature that $LaFeO_3$ exhibits canted anti-ferromagnetic behavior of G-type [35], where the anti-parallel Fe^{3+} spins interact via the oxygen ions (superexchange reactions). The canting of these spins at small angles due to exchange coupling results in a small net magnetic moment (0.031 at 2.5 K) for the undoped $LaFeO_3$ compound (Table 3). The substitution of Ag into $LaFeO_3$ results in charge instability in the oxide compound. To compensate for the charge or to maintain charge neutrality, Fe^{3+} ions are oxidized to Fe^{4+}. Our attempts to determine Fe^{4+} content by chemical titrations were not successful since during the process for preparing the compound for iodometry titration, there is a precipitation formation.

The Fe^{4+} ion has four electrons in the 3d shell (with a total spin S of 2), whose spins are anti-parallel with the corresponding Fe^{3+} spins. The difference in magnetic moment in the Fe^{3+} ($S=5/2$) and Fe^{4+} ($S=2$) leads to:

$$\mu_1 = \mu_1 \mathrm{Cos}\theta_1 - \mu_2 \mathrm{Cos}\theta_2 \quad (4)$$

where: $\mu_1 = 5.85\,\mu B$, the effective magnetic moment calculated from $g\sqrt{S(S+1)}$, $\mu_2 = 4.20\,\mu B$ the effective magnetic moment of the Fe^{4+} ions, and θ_1 and θ_2 are the canting angles.

Accordingly μ_{net} increased to 0.491 for the $x=0.3$ compound. Thus the increase in the χ observed in Fig. 9(a) and the magnetization in Fig. 8b originate from the increase in Fe^{4+} ions in the (La, Ag) FeO_3 system.

3.9. Changes in structural features

When Ag is doped into $LaFeO_3$, significant structural changes occur. Trivalent La ions with ionic radii ($r_{La}{}^{3+} = 1.36$ Å) are replaced with smaller, monovalent Ag ions whose ionic radii ($r_{Ag+} = 1.28$ Å) [36] are reflected in the lattice parameter changes (Fig. 10a). Also the unit cell volume decreases from 242.562 Å^3 to 240.614 Å^3 (Fig. 10b). The decrease in cell volume can be correlated with increasing Fe^{4+} content, as the size of Fe^{4+} is smaller than Fe^{3+} (0.53 Å vs. 0.645 Å). This effect is similar to the effect of Ca doping into $PbTiO_3$ [37].

The building block of $LaFeO_3$ perovskite is FeO_6 octahedra which are linked to form the 3D structure (Fig. 11). As Ag is introduced into $LaFeO_3$ the bond lengths and bond angles change to accommodate the doping. Accordingly, the in-plane distance $Fe_1–O_2{}'$ of the FeO_6 octahedra decreases from 1.9995 Å ($x=0$) to 1.9674 Å ($x=0.3$). The apical distance ($Fe_1–O_1$) decreases from 2.0062 Å to 2.0032 Å in a similar fashion. The in-plane bond angle $Fe–O_2–Fe$ decreases from 156.579° to 156.206° for Ag doping up to 20%. Similarly, the co-operative tilting of FeO_6 octahedra resulted in overall apical bond angles $Fe–O_1–Fe$ changes from 156.166° to 155.674°.

The increase in orthorhombic distortion as a result of Ag doping can be understood from the changes in geometric tolerance factor t for the perovskite compounds. Also, the bond angle $\theta_{Fe–O–Fe}$ is a measure of the tilting of the octahedra, and is also directly linked to orthorhombic cell distortion [38]. The tolerance factor t is a geometrical factor characterizing the size mismatch that occurs when a site cation is too small to be accommodated into the BO_6 octahedra of the three dimensional network calculated from the formula:

$$t = \frac{r_A + r_O}{(r_B + r_O)} \quad (5)$$

where r_A is the average ionic radii of the La^{3+} and Ag^+ ions, r_O is the ionic radius of the O^{2-} ion, and r_B is the average ionic radius of the Fe^{3+} and Fe^{4+} ions. The relation is such that when t decreases θ decreases and orthorhombic cell distortion increases.

For the undoped sample, $t = 0.948$ and with progressive Ag doping it decreased to 0.943 (10%, Ag), 0.937 (20%, Ag), and 0.932 (30%, Ag) [39]. As t approaches unity, the perovskite compounds will have an ideal structure with minimum structure instability.

3.10. Potential applications of (La, Ag) FeO_3 orthoferrites

The effect of Ag doping into $LaFeO_3$ has positioned the orthoferrite material for possible technological applications such as solid oxide fuel cells (SOFCs) and photocatalysts. For example, a perovskite-oxide like $LaMnO_3$ is pursued as a cathode material for SOFCs. However, Sr doped $LaMnO_3$ exhibits only “electronic conductivity” – lacking in oxide ion vacancies and the associated oxide ion conduction, thus forcing use of a thick porous electrode of the material. In essence, the performance of the cathode, thus depends on the engineered microstructure. Therefore, perovskite-oxide

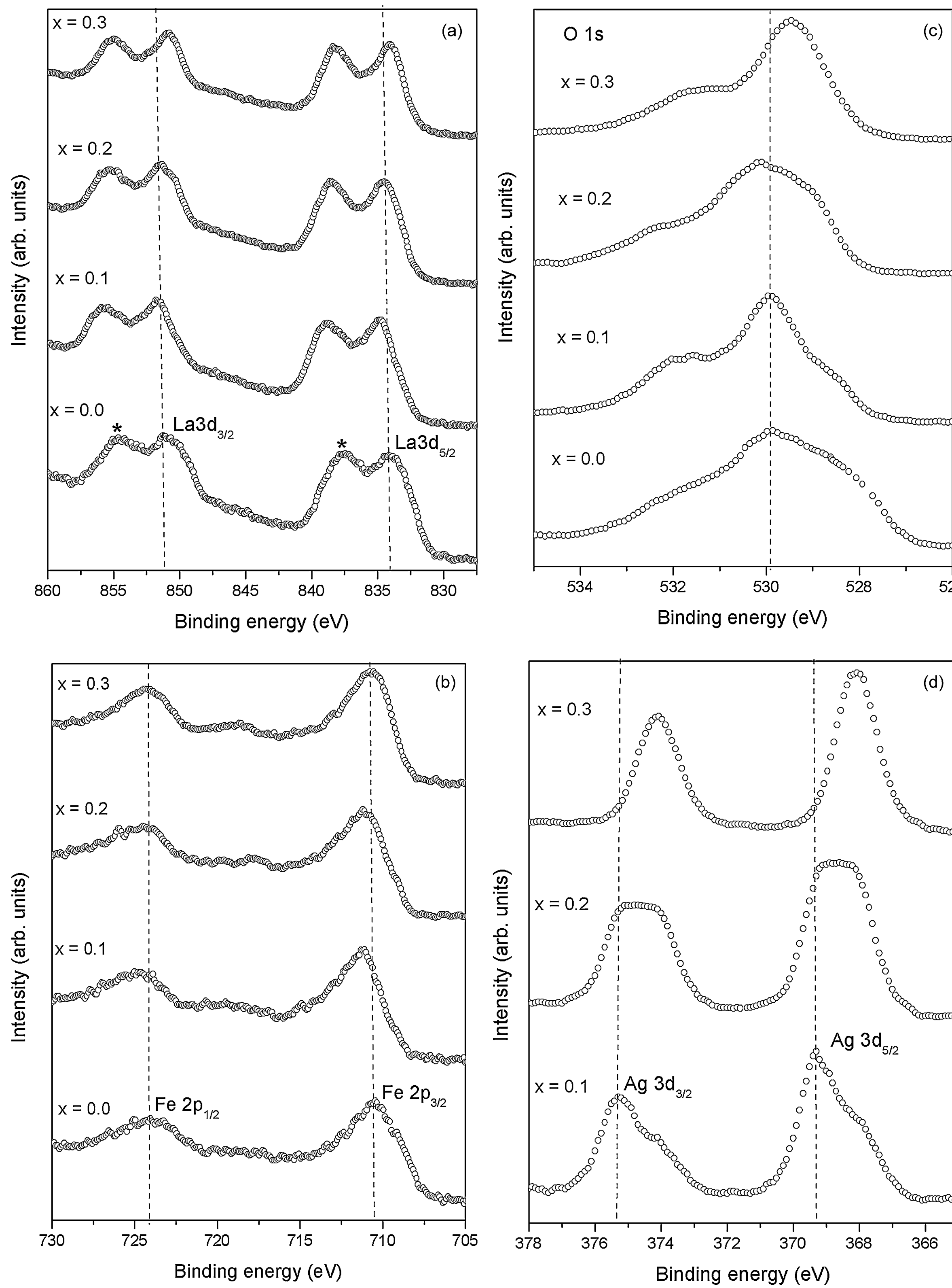

Fig. 6. XPS core-level spectra of (a) La 3d, (b) Fe 2p, (c) O 1s, and (d) Ag 3d orbit for $La_{1-x}Ag_xFeO_3$ ($0.0 \le x \le 0.3$) phases.

existing-ion conduction (i.e., electronic + ionic) is preferred and accordingly Sr and Ni doped $LaCoO_3$ and $LaFeO_3$ have been shown to be promising cathode materials [16]. Ag-doped $LaFeO_3$ materials could exhibit mixed conduction with a significant amount of Fe^{4+}, and in combination with a sufficient number of oxygen vacancies (oxygen stoichiometry decreased from 3.02 to 2.75 for $x = 0.3$ Ag doping), resulting in mixed-ion conduction, can position the material as an attractive cathode material for SOFC applications.

Among various semiconductor photocatalytic materials TiO_2 has been found to be very promising due to low cost, stability, and

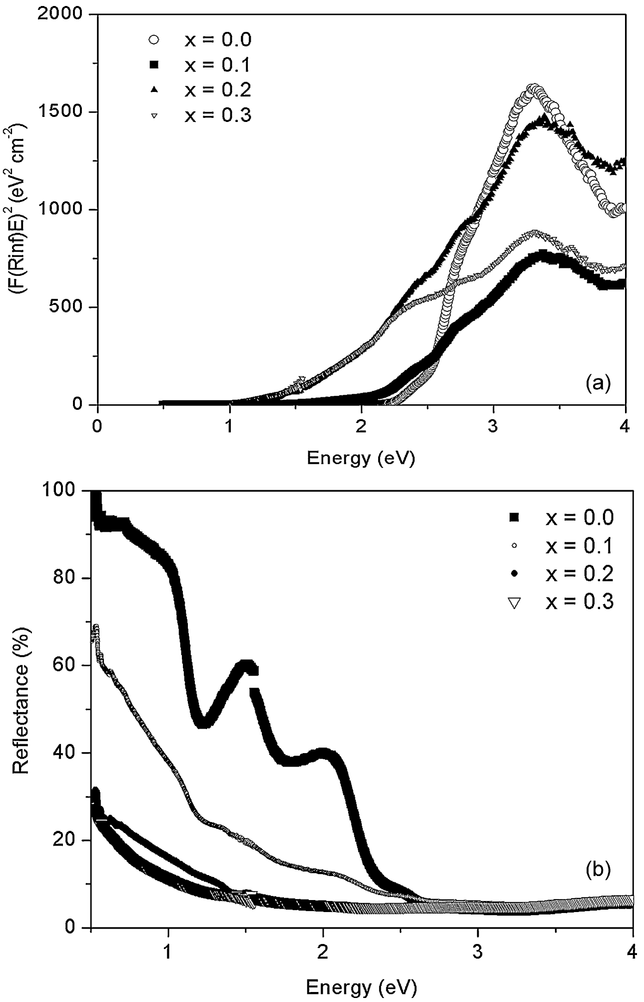

Fig. 7. (a) UV–vis absorption, and (b) Diffuse reflectance spectra, of $La_{1-x}Ag_xFeO_3$ ($0.0 \le x \le 0.3$) perovskite-oxides.

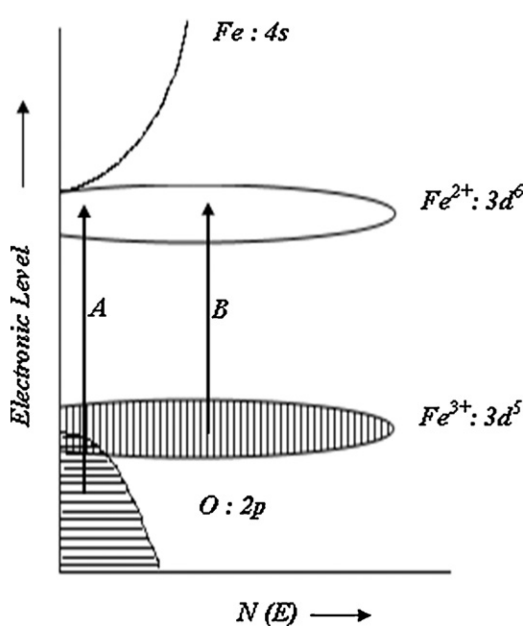

Fig. 8. Schematic band structure of a perovskite-type ferrite with octahedral structure. A and B indicate the CT transitions discussed in the text.

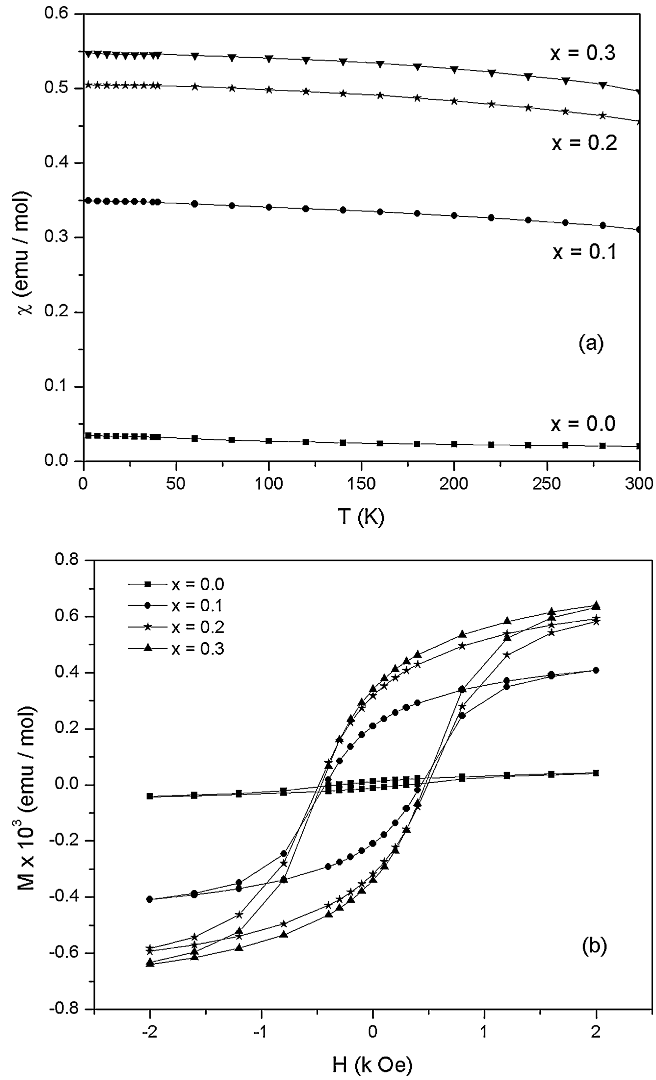

Fig. 9. (a) Molar magnetic susceptibility (χ_m) vs. temperature as a function of applied field, and (b) Hysteresis loop measured at 25 K, for $La_{1-x}Ag_xFeO_3$ ($0.0 \le x \le 0.3$) phases.

favorable electronic and optical properties. However, the efficiency of light conversion is found to be low due to the wide band gap of 3.2 eV. Perovskite materials like $LaFeO_3$ are emerging as possible replacements. S. Li et al. [40] have studied the photoinduced charge property of nanostructural $LaFeO_3$ and its photocatalytic activity for degrading Rhodamine B under visible light, and showed that the photocatalytic activity of nanostructural $LaFeO_3$ is better than that of P-25 TiO_2 nanostructural material. The band gap measured for the undoped $LaFeO_3$ nanostructural material in this study is 2.4 eV, which is lower than that of TiO_2. The band gaps of Ag-doped nanostructural material are in the same range and it is possible that these materials could have similar photo catalytic properties. Also it was shown by Choudhary et al. that Ag doping in $LaFeO_3$ has resulted in large increases in catalytic activity [41], implying the properties of the $LaFeO_3$ perovskite can be beneficial with Ag substitution at La site. Similar results were reported by Burckhardt et al. on Ag-doped $LaFeO_3$ materials [42].

4. Conclusions

(La, Ag)FeO_3 nanostructural orthoferrite synthesis has been achieved by a simple solution – based combustion process. Prop-

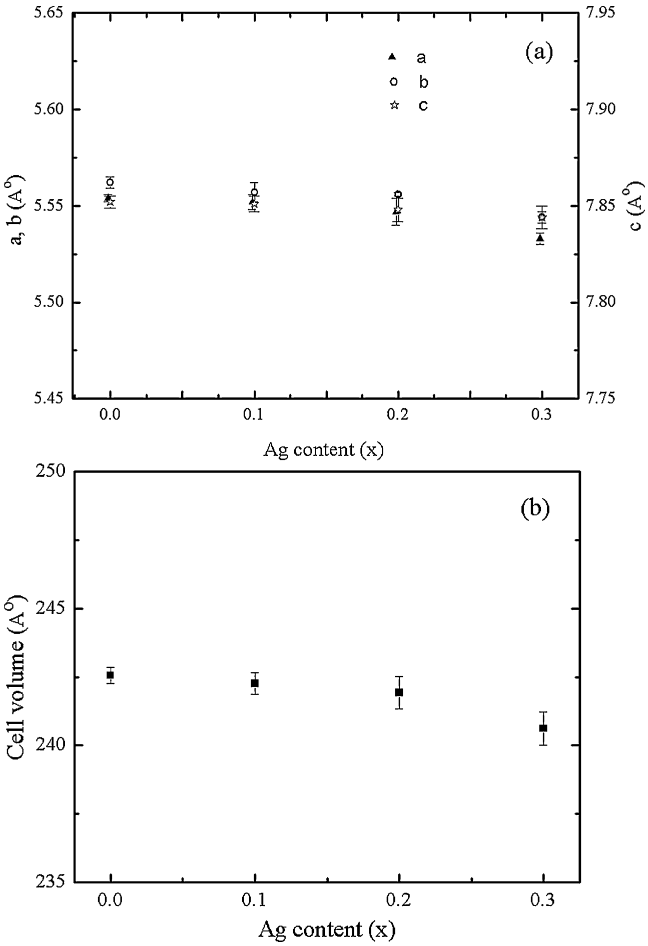

Fig. 10. (a) Plot of lattice parameter *a*, *b*, and *c* vs. Ag content, and (b) cell volume vs. Ag content.

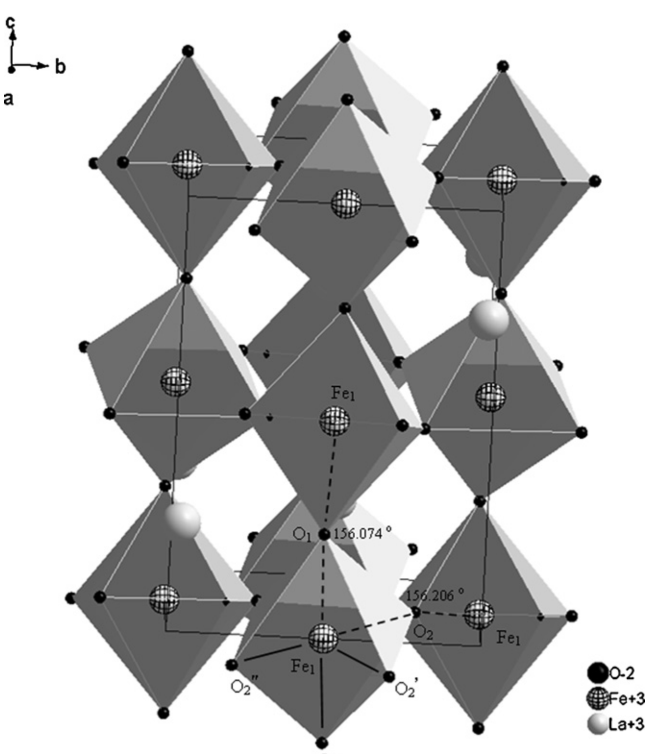

Fig. 11. Typical schematic drawing of tilted FeO_6 octahedra in $La_{0.8}Ag_{0.2}FeO_3$.

erty relationships for the synthesized materials were established by scores of experimental techniques. Structural distortion due to Ag doping is correlated to the geometric tolerance factor *t*. The observed changes in magnetic properties are correlated to creation of ions of mixed valency (Fe^{3+}/Fe^{4+}), which increase with increasing Ag doping. The optical band gaps of the (La, Ag) FeO_3 material were determined. The mixed electronic conduction of these materials, in conjunction with favorable electronic band structure could position them for SOFC and photo catalytic applications.

Acknowledgements

The authors would like to acknowledge Prof. Allan Kirkpatrick, Head, Department of Mechanical Engineering, Colorado State University, for his continued help, encouragement, and support.

References

[1] N. Kuhn, U.S. Ozkan, Catal. Lett. 121 (3–4) (2008) 179.
[2] S. Petrovic, A. Terlecki-Baricevic, L. Karanovic, P. Kirilov-Stefanov, M. Zdujic, V. Dondur, D. Paneva, I. Mitov, V. Rakic, Appl. Catal. B: Environ. 79 (2) (2008) 186.
[3] F. Bidrawn, S. Lee, J.M. Vohs, R.J. Gorte, J. Electrochem. Soc. 155 (7) (2008) 660.
[4] M.H. Hung, M.V. Madhava Rao, D.S. Tsai, Mater. Chem. Phys. 101 (2–3) (2007) 297.
[5] L. Xing, C. Bin, H. Jifan, Q. Hongwei, J. Minhua, Sens. Actuators B: Chem. B129 (1) (2008) 53.
[6] D. Bayraktar, F. Clemens, S. Diethelm, T. Graule, V.H. Jan, P. Holtappels, J. Euro. Ceram. Soc. 27 (6) (2007) 2455.
[7] E. Peter, D. Peter, V. Arvind, Chem. Eng. Sci. 61 (16) (2006) 5328.
[8] J.B. Smith, T. Norby, Solid State Ionics 177 (7–8) (2006) 639.
[9] A.D. Jadhav, A.B. Gaikwad, V. Samuel, V. Ravi, Mater. Lett. 61 (10) (2007) 2030.
[10] C. Matei, D. Berger, S. Stoleriu, F. Papa, V. Fruth, J. Optoelectronics Adv. Mater. 9 (6) (2007) 1793.
[11] S. Maike, A. Leifert, U. Simon, Adv. Funct. Mater. 17 (2007) 2189.
[12] G. Pecchi, P. Reyes, R. Zamora, C. Campos, L.E. Cadus, B.P. Barbero, Catal. Today 133 (2008) 420.
[13] W. Zheng, R. Liu, D. Peng, G. Meng, Mater. Lett. 43 (1–2) (2000) 19.
[14] X.P. Dai, Q. Wu, R.J. Li, C.C. Yu, Z.P. Hao, J. Phys. Chem. B 110 (51) (2006) 25856.
[15] A.E. Giannakas, A.K. Ladavos, P.J. Pomonis, Appl. Catal. B: Environ. 49 (2004) 147.
[16] K. Huang, H.Y. Lee, J.B. Goodenough, J. Electr. Chem. Soc. 145 (1998) 3220.
[17] T. Mimani, K.C. Patil, Mater. Phys. Mech. 4 (2001) 1.
[18] T.V. Anuradha, S. Ranganathan, T. Mimani, K.C. Patil, Scripta Mater. Ionics 111 (1998) 45.
[19] D.B. Wiles, R.A. Young, J. Appl. Crystallogr. 14 (1981) 149.
[20] A. Davydov, Infrared Spectroscopy of Adsorbed Species on the Surface of transition Metal Oxides, Wiley, England, 1990 (Chapter 1).
[21] Y.H. Lee, J.M. Wu, J. Crystal Growth 263 (2004) 436.
[22] X. Guo, Z. Chen, D. Cui, Y. Zhou, H.Z. Huang, H.X. Zhang, F. Liu, K. Ibrahim, H. Qian, J. Crystal Growth 219 (2000) 404.
[23] D.F. Mullica, C.K.C. Lok, H.O. Perkins, Phys. Rev. B 31 (6) (1985) 4039.
[24] S.J. Oh, G.H. Kim, G.A. Sawatzky, H.T. Jonkman, Phys. Rev. B 37 (1988) 145.
[25] Z. Yang, Y. Huang, B. Dong, H.L. Li, Mater. Res. Bull. 41 (2006) 274.
[26] J.F. Moulder, W.F. Stickle, P.E. Sobol, K.D. Bomben, Handbook of X-ray photoelectron spectroscopy, Physical electronics, Inc., Eden Prairie, Minnesota USA, 1995.
[27] P. Kubelka, F. Munk, J. Tech. Phys. 12 (1931) 593.
[28] G. Kortum, Reflectance Spectroscopy Principles Methods, Applications, Spinger-Verlag, New York, 1969.
[29] D.G. Barton, M. Shtein, R.D. Wilson, S.L. Soled, E.J. Iglesia, Phys. Chem. B 103 (1999) 630.
[30] J. Tauc, R. Grigorov, A. Vancu, Phys. Status Solidi 15 (1966) 627.
[31] M.R. Hoffmann, S.T. Martin, W. Choi, D.W. Bahnemann, Chem. Rev. 95 (1995) 69.
[32] B.R. Sahu, L. Kleinman, Phys. Rev. B 69 (2004) 165202.
[33] W.H. Knausenberger, R.N. Tauber, J. Electrochem. Soc. 120 (1973) 927.
[34] T. Arima, Y. Tokura, Phy Rev. B 48 (1993) 17006.
[35] I.R. Shein, K.I. Shein, V.L. Kozhevnikov, A.L. Ivanovskii, Phys. Solid State 47 (2005) 2082.
[36] R.D. Shannon, Acta Crystallogr. A 32 (1976) 751.
[37] S. Shirasaki, K. Takahashi, K. Manabe, Bull. Chem. Soc. Jpn. 44 (1971) 3189.
[38] M.A. Ahmed, S.I. El-Dek, Mater. Sci. Eng. B 128 (2006) 30.
[39] X.P. Dai, R.J. Li, C.C. Yu, Z.P. Hao, J. Phys. Chem. B 110 (2006) 22525.
[40] L. Shudan, J. Liqiang, F. Wei, Y. Libin, X. Baifu, F. Honggang, Mater. Res. Bull. 42 (2007) 203.
[41] V.R. Choudhary, B.S. Uphade, S.G. Pataskar, Fuel 78 (1999) 919.
[42] W. Burckhardt, F. Froehlich, F. Seifert, Key Eng. Mater. 132–136 (1997) 775.